


OPEN ACCESS

Transition Metal Dissolution and Degradation in NMC811-Graphite Electrochemical Cells

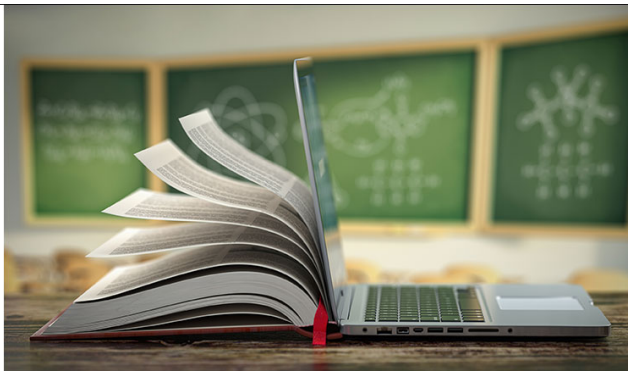
To cite this article: Zachary Ruff *et al* 2021 *J. Electrochem. Soc.* **168** 060518

View the [article online](#) for updates and enhancements.

 The Electrochemical Society
Advancing solid state & electrochemical science & technology
2021 Virtual Education

Fundamentals of Electrochemistry:
Basic Theory and Kinetic Methods
Instructed by: **Dr. James Noël**
Sun, Sept 19 & Mon, Sept 20 at 12h–15h ET

Register early and save!





Transition Metal Dissolution and Degradation in NMC811-Graphite Electrochemical Cells

Zachary Ruff,^{1,2} Chao Xu,^{1,2} and Clare P. Grey^{1,2,*}

¹Department of Chemistry, University of Cambridge, Cambridge, United Kingdom

²The Faraday Institution, Quad One, Harwell Science and Innovation Campus, Didcot, United Kingdom

Nickel-rich lithium nickel-manganese-cobalt oxide cathodes, in particular $\text{Li}(\text{Ni}_{0.8}\text{Mn}_{0.1}\text{Co}_{0.1})\text{O}_2$ (NMC811), are currently being commercialized as next generation cathode materials, due to their increased capacities compared to current materials. Unfortunately, the higher nickel content has been shown to accelerate cell degradation and a better understanding is needed to maximize cell lifetimes. NMC811/graphite cells were tested under stressed conditions (elevated temperature and cell voltages) to accelerate degradation focusing on transition metal (TM) dissolution from the cathode. Increasing the cell temperature, upper cut-off voltage (UCV) and number of cycles all accelerated capacity fade and diffraction studies showed that under stressed conditions, additional degradation mechanisms beyond lithium loss to the SEI are present. Significant TM dissolution and subsequent deposition on the graphite anode is seen, particularly at stressed conditions. The concentration of TMs in the electrolyte remained invariant with cycling conditions, presumably reflecting the limited solubility of these ions and emphasizing the role that TM deposition on the anode plays in continuing to drive dissolution. Significant deposits of metals from the cell casings and current collectors were also detected at all cycling conditions, indicating that corrosion and metal leaching can be as important as TM dissolution from the active material in some cell formats.

© 2021 The Author(s). Published on behalf of The Electrochemical Society by IOP Publishing Limited. This is an open access article distributed under the terms of the Creative Commons Attribution Non-Commercial No Derivatives 4.0 License (CC BY-NC-ND, <http://creativecommons.org/licenses/by-nc-nd/4.0/>), which permits non-commercial reuse, distribution, and reproduction in any medium, provided the original work is not changed in any way and is properly cited. For permission for commercial reuse, please email: permissions@iopublishing.org. [DOI: [10.1149/1945-7111/ac0359](https://doi.org/10.1149/1945-7111/ac0359)]



Manuscript submitted March 9, 2021; revised manuscript received May 4, 2021. Published June 21, 2021.

Supplementary material for this article is available [online](#)

Nickel-rich lithium nickel-manganese-cobalt oxide cathodes (NMC) are currently under development as next generation high-energy cathode materials for lithium ion batteries due to the material's relatively high capacity when coupled with a graphite anode.¹ However, nickel-rich NMC cathodes suffer from capacity fade during electrochemical cycling, which has been correlated to degradation observables including increased cell polarization,^{2,3} gas evolution at the electrodes,^{4,5} corrosion of the current collectors⁶ and transition metal (TM) dissolution from the cathode.^{7–10} TM dissolution is of particular interest as (1) it causes a direct loss of active materials and (2) metal ions have been shown to migrate through the electrolyte and deposit onto the anode.^{7–9} The deposited metals have been proposed to catalyze further electrolyte solvent reduction, resulting in further trapping of lithium ions at the anode in the form of the salts that comprise the degradation products that make up the solid electrolyte interface (SEI).^{7,11,12} This enhanced lithium loss is the leading explanation for why TM dissolution leads to full cell capacity fade greater than what would be expected from the loss of cathode active material alone.^{7,10,11}

The mechanism of TM dissolution in metal oxide cathodes is still not well understood and it has been proposed to occur via disproportionation reactions,¹³ leaching due to acidic species,⁷ chelation by organic ligands¹⁴ and as a consequence of oxygen loss.⁴ The increased amount of TM dissolution observed when cycling to higher upper cut-off voltages^{9,15} (UCV) suggests that TM dissolution is at least correlated to electrolyte oxidation,¹⁶ lattice oxygen release,⁴ and possibly to layered to rock salt phase transitions at the surface of cathode particles.¹⁷ Moreover, many chemical reactions that occur at high UCVs are believed to have a knock-on effect. For example, singlet oxygen released from NMC is thought to oxidize the electrolyte solvent (e.g., ethylene carbonate), generating water^{4,16} that subsequently results in lithium hexafluorophosphate, LiPF_6 , hydrolysis and the formation of hydrofluoric acid (HF).¹⁸

Although there is almost an order of magnitude more nickel than manganese in $\text{Li}(\text{Ni}_{0.8}\text{Mn}_{0.1}\text{Co}_{0.1})\text{O}_2$ (NMC811), it is believed

that the manganese dissolution is particularly detrimental to cell performance.^{7,10,19} Joshi et al. showed that adding a high concentration of soluble nickel, manganese and cobalt salts to the electrolyte causes a thickening of the SEI and leads to faster capacity fade.¹¹ The authors proposed that TM deposition on the anode initiates a catalytic cycle of TM reduction and oxidation, trapping lithium ions in the SEI and causing faster capacity fade than would be expected from the TM reduction alone. Later, Leung¹² performed theoretical calculations that supported the catalytic role of manganese for solvent reduction at the anode. Solchenbach et al.¹⁹ showed experimentally that adding a high concentration of soluble manganese salts to the electrolyte caused the continuous formation of ethane, a marker for SEI formation, upon cycling, while samples with nickel salts or only the pristine electrolyte evolved ethane only during the first cycle.

There remains a debate over the practical importance of TM dissolution and capacity fade due to lithium trapping in optimized cells. In NMC532/graphite cells, Gilbert et al.⁷ reported that the concentration of manganese measured at the graphite had a linear relationship of $\sim 1:100$ with the amount of trapped lithium at the anode in coin cells. However, work of Thompson et al.⁹ reported that the capacity loss was not well correlated with TMs at the graphite in small format pouch cells. They proposed that the different results likely could be attributed to cell optimization, including the use of single crystal NMC particles and electrolyte additives.

As NMC811 cells approach commercialization,¹ a challenge for academic labs is how to study relevant cell degradation processes over weeks/months rather than years.²⁰ Here, we cycle cells under “stressed” or “aggressive” cycling conditions (increased temperature and upper cut-off voltage) to accelerate cell degradation and TM dissolution to study their effects on cell capacity fade with the understanding that these conditions exceed normal expected use conditions of most NMC811 cells. Nevertheless, we emphasize that certain stress conditions are highly relevant to the practical use of cells, for instance, elevated temperature cycling and storage are widely acknowledged to occur in large-scale cells due to inhomogeneous and/or insufficient cooling. We also employ bespoke “flooded” Swagelok T-cells (Fig. 1) to quantify the TMs in the electrolyte, on the separators and on the graphite anode separately to gain insight into the metal dissolution, migration, and deposition

*Electrochemical Society Fellow.

^zE-mail: cpg27@cam.ac.uk

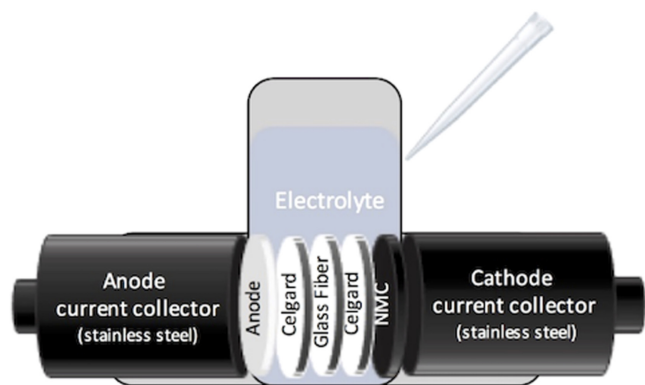


Figure 1. Flooded Swagelok cell with electrolyte that can easily be extracted for further analysis.

processes. After ageing at various conditions, the metal content of each component is measured using inductively coupled plasma optical emission spectroscopy (ICP-OES). The results from the Swagelok cells then are compared to coin and pouch cells aged under the same conditions.

We show that increasing the cell ageing temperature, UCV and number of cycles each led to a higher mass of TM deposits on the graphite anode, while the masses of TMs in the electrolyte were invariant with cycling conditions. To separate capacity fade due to lithium loss in the SEI from capacity fade due to, for example, cell polarization, we compare measurements of the cathode state of charge (SoC) using X-ray diffraction²¹ with the capacity loss calculated from electrochemical data, showing good correlations between the two techniques for cells aged under less extreme conditions, indicating that lithium loss at the anode is the dominant source of capacity fade. At stressed conditions, we find worse correlation, originating from additional contributions to capacity fade, for instance, increased cell polarization. We also measure metals from the cell body and current collectors for all cycling conditions in Swagelok and coin cells, highlighting the sometimes overlooked importance of corrosion from electrochemically inactive components. This study provides additional insight into TM dissolution's impact on cell degradation and helps to identify conditions where more mechanistic studies of TM metal dissolution can be performed in the future.

Experimental

Cell materials.—NMC811 and graphite printed electrode foils were provided by the Cell Analysis, Modeling and Prototype (CAMP) facility at Argonne National Lab (USA). Details of the cathode electrode can be found in the report by Rodrigues et al.⁸ Briefly, the NMC cathode (batch code A-C020) consists of 90 wt% NMC811 (Targray), 5 wt% PVDF binder (Solvay 5130) and 5 wt% carbon black (Timcal C45) coated on an aluminum current collector with a mass loading (active material) of 8.3 mg cm⁻². The graphite electrode is composed of 91.83 wt% graphite powder (Hitachi MagE3), 2 wt% carbon black (Timcal C45), 6 wt% PVDF binder (Kureha 9300) and 0.17 wt% oxalic acid and is coated on a copper current collector with a mass loading of 5.8 mg cm⁻². The negative to positive capacity ratio is ≈1.31, estimated based on a practical capacity of 195 mAh g⁻¹ for NMC811 and 360 mAh g⁻¹ for graphite.

The electrolyte consists of 1.0 M LiPF₆ salt in a mixed ethylene carbonate (EC) and ethyl methyl carbonate solvent (EMC) in 3:7 w/w (LP57, Soulbrain, USA) without additional additives. Both glass fiber (GF/B, Whatman) and polymer (Celguard, 3501) separators were used in the electrode stack.

Electrochemical cells.—Flooded Swagelok cells were made from 5/8" Swagelok[®] 316 stainless steel (SS) t-unions with "plunger"

current collectors machined from 316 SS (Fig. 1). The geometry of the cell is similar to a conventional Swagelok cell except that the third port of the t-union acts as a reservoir for electrolyte. 15 mm diameter cathodes and anodes (typically 14.66 mg and 10.24 mg of active material per electrode respectively) were punched from the electrode sheets and assembled in the t-unions with three layers of separator consisting of a piece of glass fiber sandwiched between two pieces of polymer (all punched to 16 mm, ~5/8", in diameter). The polymer separators at the cathode and anode sides prevent cathode and graphite particles from releasing onto or getting stuck on the glass fiber separator.

To assemble the cells, the NMC cathode, one polymer separator and the glass fiber separator were placed on the cathode plunger. Next, 100 μl of the electrolyte was added to the exposed glass fiber separator. The second Celgard separator and anode were then put in place and compressed with the anode plunger establishing good contact and stack pressure. Finally, another 900 μl of electrolyte was added via the third port in the Swagelok cell for a total of 1000 μl of electrolyte to complete the assembly. Kapton film was used to prevent the electrode contacts from shorting to the cell body.

For comparison, coin cells and pouch cells were also fabricated and tested. The coin cells used the same electrode stack as the Swagelok cell, with the three separators and 100 μl of electrolyte assembled into 2032-type cells (Cambridge Energy Solutions). Multilayer pouch cells with a double-sided electrode coating and a nominal capacity of 200 mAh were purchased dry and sealed from LiFun. The pouch cells were opened and filled with 0.9 ml of LP57 and vacuum sealed in a dry room before testing. The pouch cells consisted of the same NMC811 from Targray, but a different synthetic graphite anode, a single polymer separator and no glass fiber separator. Both the cathode and anode of the pouch cells are double-side coated and the single-side loadings of the active materials are 16.7 mg cm⁻² for cathode and 12.6 mg cm⁻² (approximately twice as high as those of the Argonne electrodes).

Measurements of the cathode and anode potentials during cycling were made using a three-electrode Swagelok cell (Fig. S1 available online at stacks.iop.org/JES/168/060518/mmedia) with a 50% delithiated lithium iron phosphate (Li_{0.5}FePO₄, LFP, carbon-coated commercial powder) reference electrode. To obtain the LFP reference electrode, a LFP cathode (90% LFP, 5% superP, 5% PVDF coated on aluminum) was delithiated in a cell against lithium metal to a 50% SoC, after which the LFP potential was measured at open circuit condition to be 3.42 V vs Li/Li⁺. A thin strip of the LFP reference electrode was clamped between two glass fiber separators soaked with 200 μl of LP57 and placed in between the graphite anode and NMC811 cathode.

Electrochemical cycling.—The three-electrode cells underwent two formation cycles at a rate of C/20, where 1 C is the current to charge/discharge the cell in 1 h to a 4.2 UCV (based on a cathode capacity of 195 mAh g⁻¹). After formation, the three-electrode cell underwent potentiostatic holds for 6 h, at each 3.0, 4.2, 4.4 and 4.6 V (full-cell) voltage with C/3 charge steps between each voltage hold, to measure the potentials of the cathode and anode separately at states of charge (SoCs) approaching equilibrium conditions.

For the ageing experiments, Swagelok, coin and pouch cells were also formed using two constant current (CC) C/20 cycles at a given UCV. The cells were then subsequently cycled galvanostatically using a CC rate of C/3 from 3.0 V to the UCV. For comparison, cells were also cycled using a constant current, constant voltage protocol (CCCV) where the cells were held at the UCV until the current decreased to < C/20 during both the ageing charge and discharge steps. The Swagelok and coin cells were tested using a Biologic VMP2 potentiostat and the pouch cells were tested in an Arbin LBT battery cycler due to the increased current required to test the higher capacity cells. The pouch cells were discharged to 2.0 V before disassembling as a safety precaution. Additional long term cycling data for the coin cells can be found in Fig. S3.

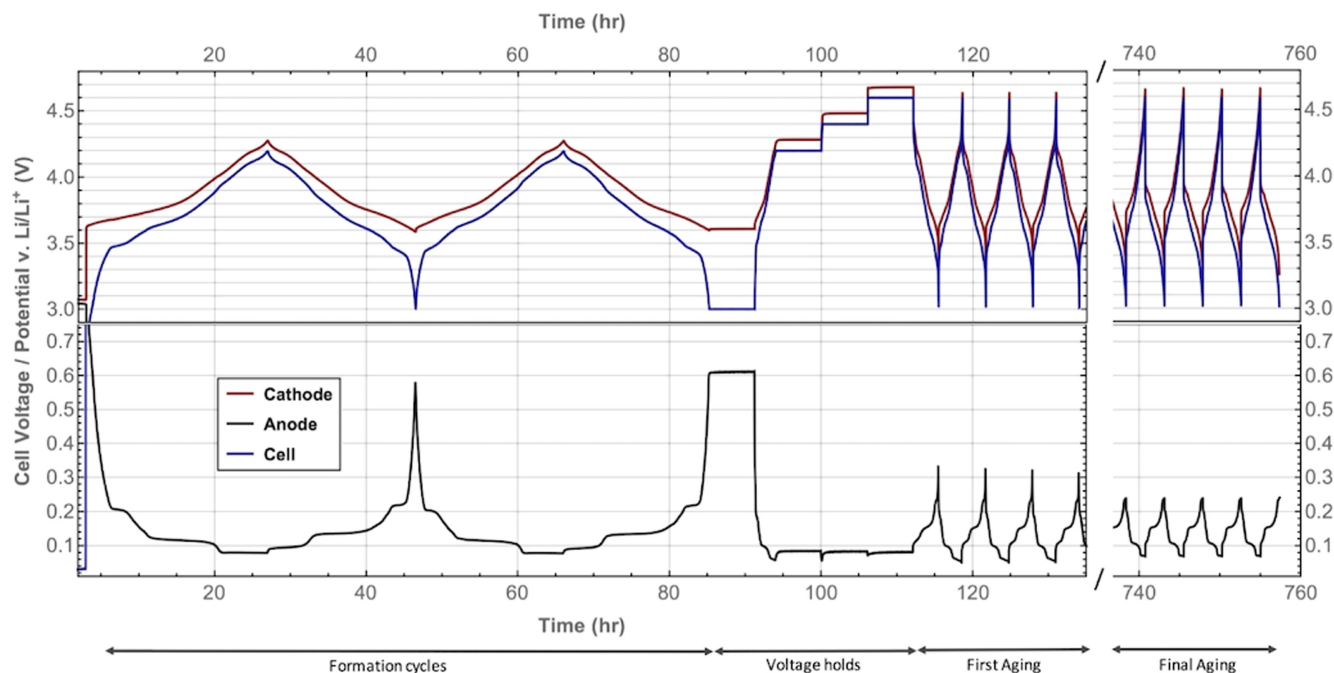


Figure 2. Cell voltage, cathode (NMC) and anode (graphite) potentials for the three-electrode cell at room temperature. The cell is first formed (two C/20 cycles), then held at 3.0, 4.2, 4.4 and 4.6 V for 6 h, before undergoing 120 cycles from 3.0 V–4.6 V. Expanded plots of the voltage profiles are in the Fig. S2.

Elemental analysis of cell components.—After cycling, the Swagelok cells were disassembled in an argon glovebox. The electrolyte was removed with a micropipette and approximately 500–700 μl of the electrolyte was recovered. The graphite anode, NMC cathode and separators were also reserved for further characterization.

Elemental analysis was performed using inductively coupled optical emission plasma spectroscopy (ICP-OES, Thermoscientific). The aged graphite anodes and separators were placed in individual borosilicate vials before adding 250 μl of concentrated nitric acid (66%–68%, trace element grade, Fisher Scientific) and 750 μl of ultra-pure water (Millipore, >10 M Ω). After three days, the digested samples were diluted to 10 ml with additional ultra-pure water and (in the case of the glass fiber separator) centrifuged before measuring using ICP-OES. To prepare the electrolyte samples, 100 μl of the extracted electrolyte was added to 10 ml of ~2% nitric acid before testing. To validate the method of sample workup for the anode, the discussed protocol was compared to results using a previously published sample preparation protocol used by the analytical facility at Argonne national lab^{7,8} (Fig. S4). This was achieved by cutting the electrodes in half, the two halves being weighed before the processing and the results scaled to the mass of a full 15 mm diameter electrode. The two methods gave similar results. The amount of metals on the anodes is reported by mass per 15 mm diameter electrode and mass per electrode area. In each 15 mm cathode, there is 7.10 mg (4.01 mg cm⁻²) of nickel, 0.89 mg (0.50 mg cm⁻²) of manganese and 0.83 mg (0.47 mg cm⁻²) of cobalt.

The concentration of a given element in the solution was determined by comparing the emission of the sample solutions to a calibration line generated from a concentration series made from a multi-element standard (VWR, Aristar[®]) at each wavelength of interest. The emission wavelengths were selected such that there was no interference from other elements in the sample, elements in the standard or the matrix solution (2% nitric acid).

SoC determination from X-ray diffraction of cathodes.—The cathodes extracted from the aged cells were rinsed with dimethyl carbonate (Sigma Aldrich) in an argon glovebox and dried under vacuum. The cathodes were then sealed between two thin Kapton[®]

films (Spex) before being measured in a laboratory X-ray diffractometer (Panalytical, Empyrean, Cu-K α radiation, non-monochromatic, $\lambda = 1.541 \text{ \AA}$). The lattice parameters were determined by Rietveld refinements against the diffraction data using TOPAS (version 4.1) software based on the α -NaFeO₂ structural model (R $\bar{3}m$ space group) with the transition metals on the 3a sites, Li on the 3b sites and O on the 6c sites. The lattice parameters were compared to those previously determined from refinements of *operando* diffraction measurements performed on half-cells at a synchrotron²¹ to correlate the lattice parameters (*cla* ratio) to the state of charge of the cathode.²²

Results

Electrode potential profiles during cycling.—The three-electrode cell was used to measure the electrode potentials during the SEI formation, quasi-equilibrium SoC conditions (voltage holds), and during ageing (Fig. 2). The difference in the potential and voltage profiles between the first and second formation cycle shows the capacity loss due to forming the SEI on the anode and any irreversible processes at the cathode. After forming the cell, the voltage was held for six hours at 3.0 V, and the cathode and anode potentials were measured to be 3.6 V and 0.6 V vs Li/Li⁺, respectively. After the voltage holds at 4.2, 4.4 and 4.6 V, the cathode potentials (4.3, 4.5 and 4.7 V vs Li/Li⁺) are ~0.1 V (80 mV) above the overall cell voltage, the difference corresponding to the potential of the graphite anode (vs Li/Li⁺) in the final stage (stage 1) of lithiation.²³ The irreversible capacity loss during formation sets the lower SoC limit of the NMC cathode and fixes the cathode potential at this lower-cutoff voltage (3.0 V) to be >3.6 V vs Li/Li⁺ for this cell balancing. The sharp feature in the anode profile at low cell voltages is due to the further delithiation of the graphite to beyond stage 4.²³

Comparing the potential profiles of the second formation cycle and first ageing cycle shows the rate dependence of the overpotentials, with the anode potential pushed lower during the faster ageing cycles (C/3 vs C/20, Fig. 2, see Fig. S2 for enlarged plot). As the cell was aged, the asymmetry between the charge and discharge profiles grew significantly, which is reflective of the increased cell polarization. The effect is particularly pronounced at the top of

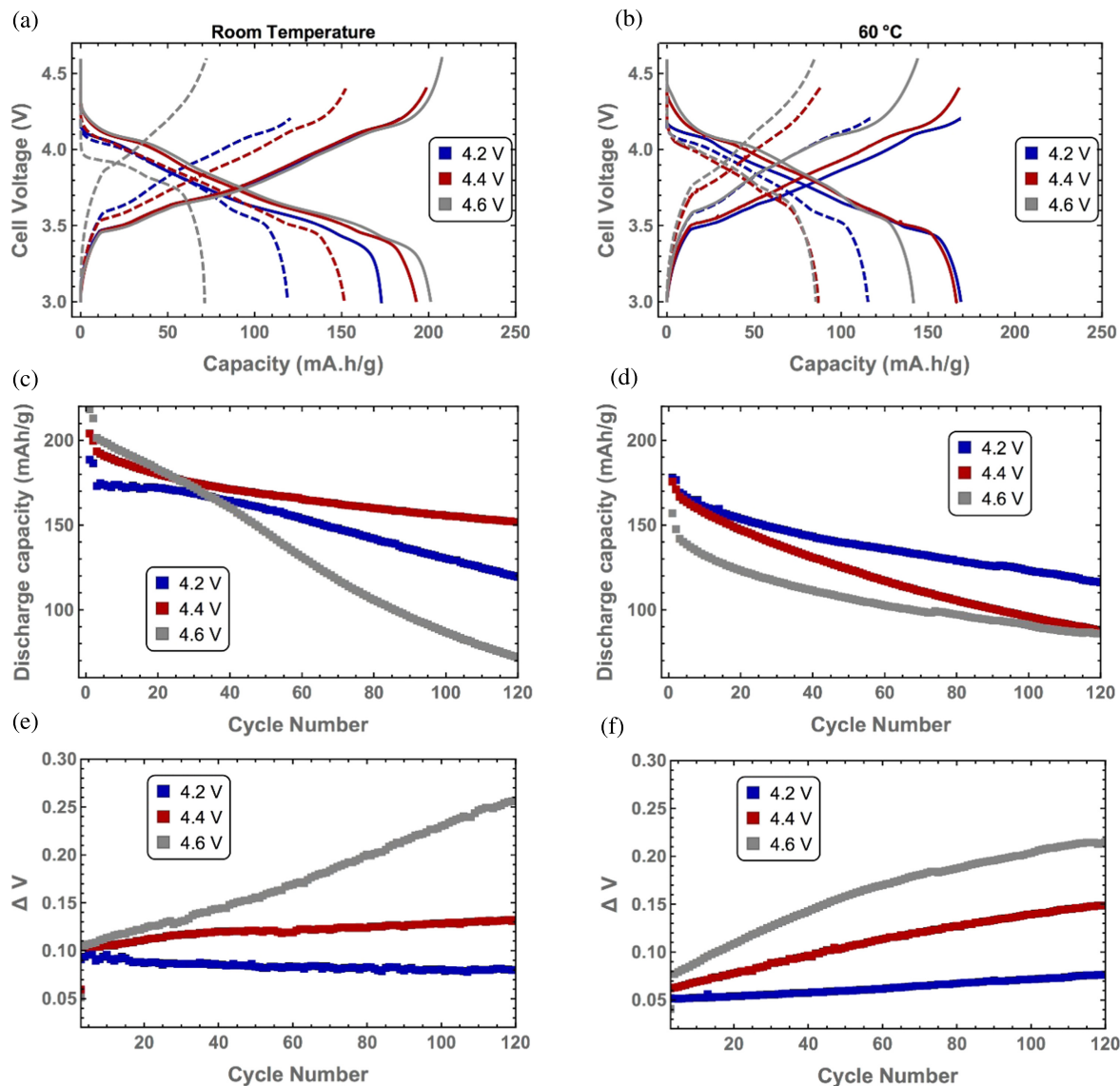


Figure 3. Voltage versus capacity profiles for the first (solid) and last (dashed) ageing cycles for the Swagelok cells aged for 120 cycles at room temperature (a) and 60 °C (b). (The 4.2 V and 4.4 V first ageing curves are difficult to distinguish in the room temperature plots as they overlap). Discharge capacity for Swagelok cells cycled at room temperature (c) and 60 °C (d). Change in the average cell potential during charging/discharging for cells cycled at room temperature (e) and at 60 °C (f). The rise in ΔV indicates increasing cell polarization over the 120 cycles.

charge, where the NMC potential drops immediately from 4.7 V to below 4.0 V at the start of the final discharge.

The capacity losses of the two-electrode, “flooded” Swagelok cells after the formation cycles are similar for all room temperature cells regardless of UCV (cells were formed and aged at the same UCV, Table I). By contrast, at 60 °C, the capacity loss after formation increases with UCV, such that the cell with the 4.6 UCV has twice the capacity loss as the cell with the 4.2 UCV, suggesting additional degradation processes at elevated temperatures.

Cell capacity fade and cell polarization.—The electrochemical performance of the Swagelok cells’ discharge capacity over 120 cycles is plotted in Fig. 3. The room temperature cells all have initial capacities that reflect the increased capacity with UCV. However, during cycling, those with a higher UCV fade much more quickly. Plots of ΔV vs cycle number, measured as the difference in the time-averaged charge and discharge voltage of the cell (see SI for calculation and Fig. S5) are shown (Figs. 3e, 3f), ΔV being a useful metric for quantifying the cell polarization.² At room temperature, the 4.2 UCV cell shows no increase in cell polarization, while the

cells cycled to 4.4 V and 4.6 V show a clear increase with cycle number.

Unlike the room temperature cells, the 60 °C cells show an initial discharge capacity on the first ageing cycle that decreases significantly with UCV. This decrease is due to an increased loss of capacity, hence a lower coulombic efficiency, during the formation cycles (Fig. 2 and Table I). During ageing, the heated cells’ capacity loss does not have a simple relationship to UCV (Fig. 3, Table I), which highlights the complexity of the ageing mechanisms at higher cell UCVs and temperatures.

To separate the various degradation processes, we compare the total capacity loss based on the electrochemistry cycling data, and the SoC or lithium concentration of the NMC811 cathode (at the discharged state), listed in Table I as x_{XRD} . Capacity loss during cycling can be attributed to multiple mechanisms, the most significant ones being lithium inventory loss due to SEI formation on the anode, cell polarization and loss of active materials.²⁴ The SoC of the cathode at the fully discharged state is a good estimate of the loss in cyclable lithium, i.e. loss of lithium inventory and is estimated here using the lattice parameters of the cathode (see

Table I. Comparison of capacity loss and lithium composition values obtained from electrochemical and diffraction methods after aging for 120 cycles. Also shown is the change in cell polarization (measured as the difference between ΔV at the end and start of cycling), which highlights the contribution of cell polarization to capacity fade.

UCV	Cycling conditions		Capacity loss from electrochemistry ^{a)}			Equivalent x-value in $\text{Li}_{1-x}\text{Ni}_{0.8}\text{Mn}_{0.1}\text{Co}_{0.1}\text{O}_2$	x in $\text{Li}_{1-x}\text{Ni}_{0.8}\text{Mn}_{0.1}\text{Co}_{0.1}\text{O}_2$ from XRD ^{b)}		XRD vs Electro-chemistry	Cell polarization (Change in ΔV)
	Temp.	Cell format	Protocol	Formation (mAh g^{-1})	Ageing (mAh g^{-1})		Total (mAh g^{-1})	x_{XRD}		
4.2	RT	Swagelok	CC	41.0	55.4	96.5	0.36	0.35	0.01	0.00
4.4	RT	Swagelok	CC	47.8	42.8	96.7	0.36	0.28	0.08	0.03
4.6	RT	Swagelok	CC	54.7	132.5	187.0	0.69	0.53	0.16	0.15
4.2	60 °C	Swagelok	CC	63.9	54.6	118.5	0.44	0.33	0.11	0.03
4.4	60 °C	Swagelok	CC	70.1	81.0	151.1	0.56	0.39	0.17	0.08
4.6	60 °C	Swagelok	CC	128.0	57.5	185.5	0.68	0.39	0.29	0.21
4.4	RT	Swagelok	CCCV	38.7	22.0	60.7	0.22	0.15	0.07	0.33
4.4	60 °C	Swagelok	CCCV	76.5	87.2	163.7	0.59	0.37	0.22	0.65
4.2	60 °C	Coin	CC	74.0	68.5	142.5	0.53	0.38	0.15	0.03
4.2	60 °C	Pouch	CC	21.5	38.4 ^{c)}	60.0 ^{c)}	0.21 ^{c)}	0.14 ^{c)}	0.07	0.28

a) The capacity loss due to formation is the charge capacity of the first formation cycle subtracted by the discharge capacity of the second formation cycle. The capacity loss due to ageing is the discharge capacity of the first ageing cycle subtracted by the discharge capacity of the final ageing cycle. The total loss is the sum of the capacity loss due to formation and ageing, from which the equivalent lithium content is obtained by dividing by the theoretical capacity of NMC811 (275.5 mAh g^{-1}). b) The diffraction method for determining lithium content used Rietveld refinements of the diffraction patterns of the cathodes after ageing (in the discharged state) and comparing the c/a parameter to refinements of *operando* measurements published elsewhere.²¹ c) The pouch cell was discharged to 2.0 V after cycling as a precaution for disassembling the cell and is therefore discharged more than the Swagelok and coin cells. The capacity loss estimate during ageing for the pouch cell includes the final discharge to 2.0 V where an additional 9.2 mAh g^{-1} of capacity was extracted (Table S1).

experimental). Note the cells here are discharged to 3.0 V, and the graphite anode is not fully delithiated at this voltage as shown by graphite potential for during the ageing cycles in Fig. 2, which is still in stage 3.²³ Thus, the x_{XRD} in Table I is an overestimation of the lithium loss, although the deviations are expected to be quite small particularly when the cell polarization is not high because the capacity (hence the amount of active lithium) from stage 3 to fully delithiated state is rather limited. Nonetheless, if the capacity fade extracted from the electrochemistry is close to the SoC of the cathode when the cell is discharged, this indicates that the capacity loss is dominated by the loss of active lithium inventory. However, if cell polarization and/or loss of active material plays a significant role, a notable deviation will be observed between the two.

Cells aged at room temperature and a UCV of 4.2 V showed a good agreement between the two techniques, indicating that the capacity loss can be mainly attributed to the loss of lithium inventory. No large increase in polarization after cycling was seen, consistent with this result (also confirmed by the voltage profile and ΔV shown in Fig. 3). A careful differential voltage (dV/dQ) analysis of coin cells (in previous work using similar NMC811/graphite cells) has shown that lithium trapping is the dominant process for these cells for approximately the first 300 cycles in cells cycled to 4.2 V, but that additional processes were seen to occur once the cathode voltage increased above 4.3 V.²⁵

As both the temperature and UCVs are increased, there is an increasing difference between the capacity loss measured electrochemically and the cathode SoC measured by diffraction at the discharged state, indicating that the capacity loss solely cannot be attributed to loss of active lithium. Indeed, increased cell polarization (ΔV , Table I, Fig. 3) is also observed and therefore assigned as the origin of the additional capacity loss at stressed conditions. Note that the loss of active lithium is overestimated more, based on x_{XRD} , when the cell suffers from more severe polarization due to incomplete graphite delithiation. Therefore, the difference between the capacity fade and active lithium loss could be even larger than what's shown in Table I, and an even larger contribution from cell polarization to the overall capacity fade is expected.

Mass of metals on graphite anodes after cycling.—A bar chart of the mass of nickel, manganese, and cobalt (referred to throughout this paper as the “cathode metals”), measured on the graphite anodes after a fixed number of cycles (120) at different temperatures and UCVs is shown in Fig. 4. There was no measurable amount of cathode metals on the graphite anode before cycling. After cycling, the mass of cathode metals on the anode increased with higher cycling temperatures and UCVs, with the cell cycled at 60 °C to a 4.6 UCV having the greatest mass of cathode metals.

To highlight the effect of cycle number and UCV, the masses of cathode metals on the anodes cycled at 60 °C are compared in Fig. 5. The mass of the cathode metals increases with cycle number, showing that the process of metal dissolution, migration and deposition is continuous during cycling. The effect of UCV is particularly pronounced. For example, the cell that only underwent the two formation cycles at 4.6 V has significantly more cathode metals at the anode ($6.1 \mu\text{g cm}^{-2}$ of Ni, $0.62 \mu\text{g cm}^{-2}$ of Mn, $0.3 \mu\text{g cm}^{-2}$ of Co), than the cell cycled to 4.2 V for 240 cycles ($1.0 \mu\text{g cm}^{-2}$ of Ni, $0.2 \mu\text{g cm}^{-2}$ of Mn, $0.1 \mu\text{g cm}^{-2}$ of Co). For context, $1 \mu\text{g cm}^{-2}$ of a metal corresponds to 0.01% of the cathode by mass or 0.03% of the nickel, 0.2% of the manganese or 0.2% cobalt of the mass of the metal in the cathode.

The dissolution behavior of the three transition metals, nickel, manganese and cobalt, is also different and dependent on the ageing conditions. Cobalt dissolves the least compared to the other two. The nickel to manganese (Ni/Mn) ratio on the anode also increases with more aggressive (increased temperature, UCV) cycling conditions (Fig. 6), while the cells cycled at room temperature have a Ni/Mn ratio that is nickel-poor compared to the cathode stoichiometry (8:1). However, once the cycling temperature is increased to 60 °C, the deposits become more nickel-rich and higher overall higher masses

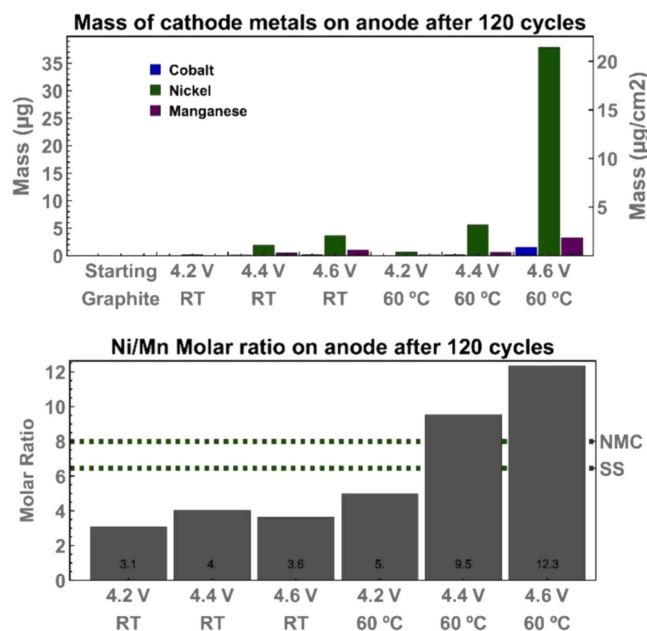


Figure 4. Mass of cathode metals on the graphite anode after 120 cycles (top) and the molar ratio of nickel to manganese on the anode (bottom). The dashed lines are the molar ratios of nickel to manganese in the cathode (NMC) and in 316 SS. The mass of metals and Ni/Mn molar ratio increases with both increased temperature and upper cut-off voltage. The numbers in black display the ratio represented in the chart.

of nickel, manganese and cobalt are measured. The deposits continue to become slightly more nickel rich as the number of cycles increases (Fig. 6), but with some variations in this trend.

There are also significant deposits of other metals observed on the anode besides nickel, manganese, and cobalt, notably aluminum, chromium, and iron (Fig. 5). Before cycling, the graphite anode also contains a small amount of these metals, particularly aluminum. Elemental analysis of the uncoated copper foil shows that the metallic impurities ascribed to the pristine graphite anode primarily come from the current collector (since the entire anode including the copper foil was dissolved together), with a minor contribution from residual impurities in the graphite and those introduced during the preparation of the electrode coating (e.g. by ball milling).

The masses of chromium and iron increase with cycle number (i.e., time), but do not seem to have a significant dependence on UCV. This result suggests that the dissolution of the stainless steel is continuous, and occurs steadily even at a cut-off potential of 4.2 V. The iron to nickel (Fe/Ni) ratio, plotted in Fig. 6 monitors the relative amount of metals from the cathode to metals from the cell components (the molar ratio of Fe/Ni in Swagelok body and plungers were measured to be 6.5 and 5.4 respectively, Fig. S6). The Fe/Ni ratio decreases drastically during aggressive cycling, consistent with an increase in cathode metals but not corrosion products from the cell component. The amount of aluminum also increases during cycling, but a clear dependence on the cycling conditions is not seen.

Transition metals in the glass fiber separator and the electrolyte.—The mass of cathode metals in the glass fiber separator and in 100 μl of electrolyte after ageing is shown in Fig. 7. 100 μl of electrolyte was chosen for comparison to the separator, since it is approximately the volume of electrolyte that wets the glass fiber separator, and a tenth of the total electrolyte in the flooded cells. There is an order of magnitude more cathode metals in the glass fiber separator than in 100 μl of the electrolyte, suggesting that either the electrolyte in the glass fiber separator is not homogenizing with the electrolyte reservoir or, more likely, that metals are precipitating/absorbing onto the glass separator. The mass of cathode metals in the

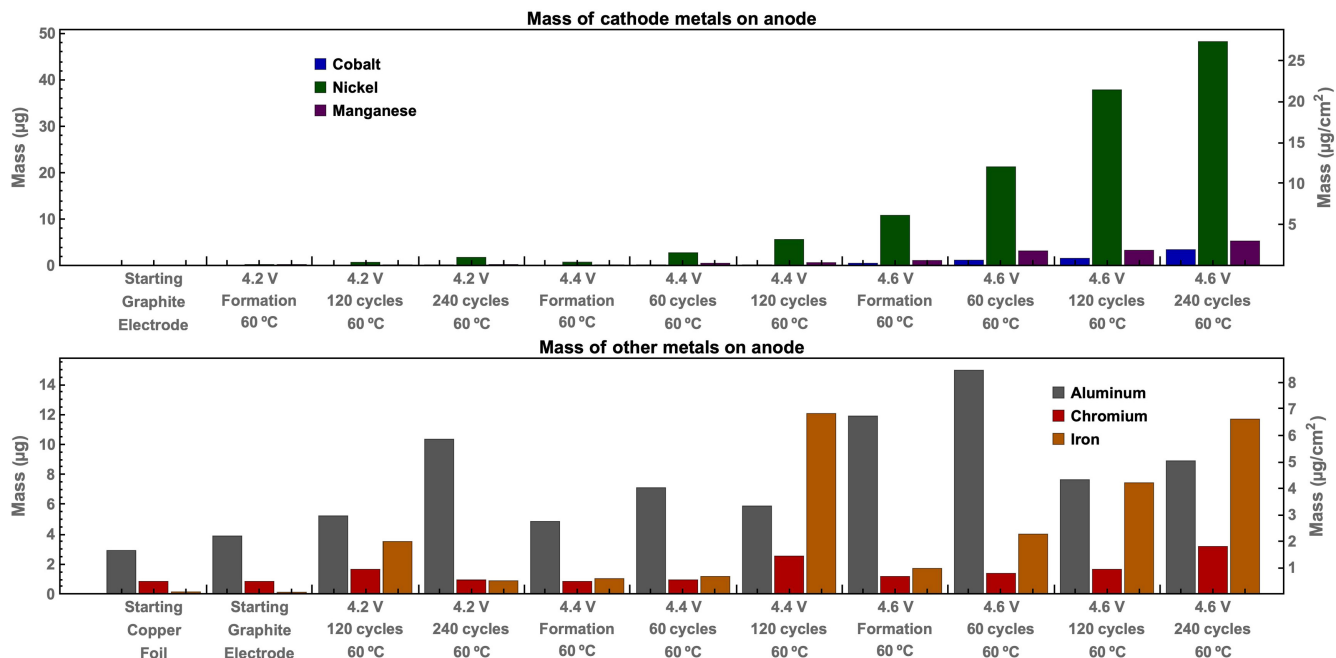


Figure 5. Mass of cathode metals on the graphite anode after electrochemical cycling at 60 °C as a function UCV and cycle number (top). Mass of metals from other cell components, aluminum, chromium and iron for the same cells (bottom).

separator slowly increases with cycle number, suggesting a continuous precipitation of metals during cycling. The total mass of metals in the electrolyte is 10 times the mass plotted in the bottom of Fig. 7, assuming that a negligible amount of electrolyte was consumed during cycling. Therefore, the total mass of metals in the electrolyte in these cells is at the µg level.

We note that contamination from cathode particles getting stuck on the glass fiber separator (particularly on disassembly of the battery) was prevented by adding a polymer separator layer between the cathode and the glass fiber. The mass of metals measured on the “cathode” polymer separator placed between the glass fiber separator and the cathode are shown in the supporting information (Fig. S7)

and are stoichiometric with respect to NMC811 and show no clear dependence on cycling conditions.

Cycling conditions: CC vs CCCV.—To explore the effect of cell polarization further, Swagelok cells also are cycled at either room temperature or 60 °C to a 4.4 UCV, using a CCCV protocol (Fig. 8a). The room temperature cell shows significantly less discharge capacity fade than the cell cycled using CC. This result was expected, since the voltage hold mitigates the apparent capacity loss seen in a CC experiment caused by any cycling induced increase in cell polarization. Of particular note, the cells cycled with the voltage hold have significantly more cathode metals at the anode

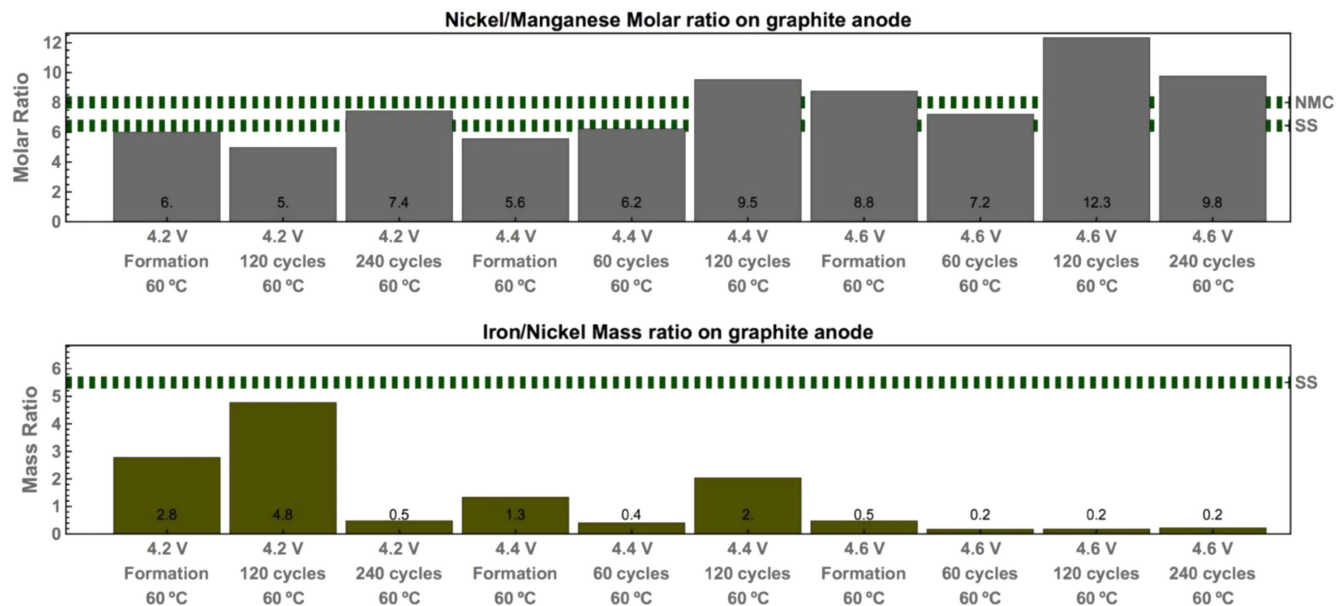


Figure 6. Molar ratio of nickel to manganese on graphite anode (top). Dashed lines represent the molar ratio of nickel to manganese (NMC) in NMC811 and 316 stainless steel (SS). Mass ratio of iron to nickel on graphite anode (bottom). Dashed line is the mass ratio of nickel to manganese in 316 stainless steel. The numbers display the ratio represented in the chart.

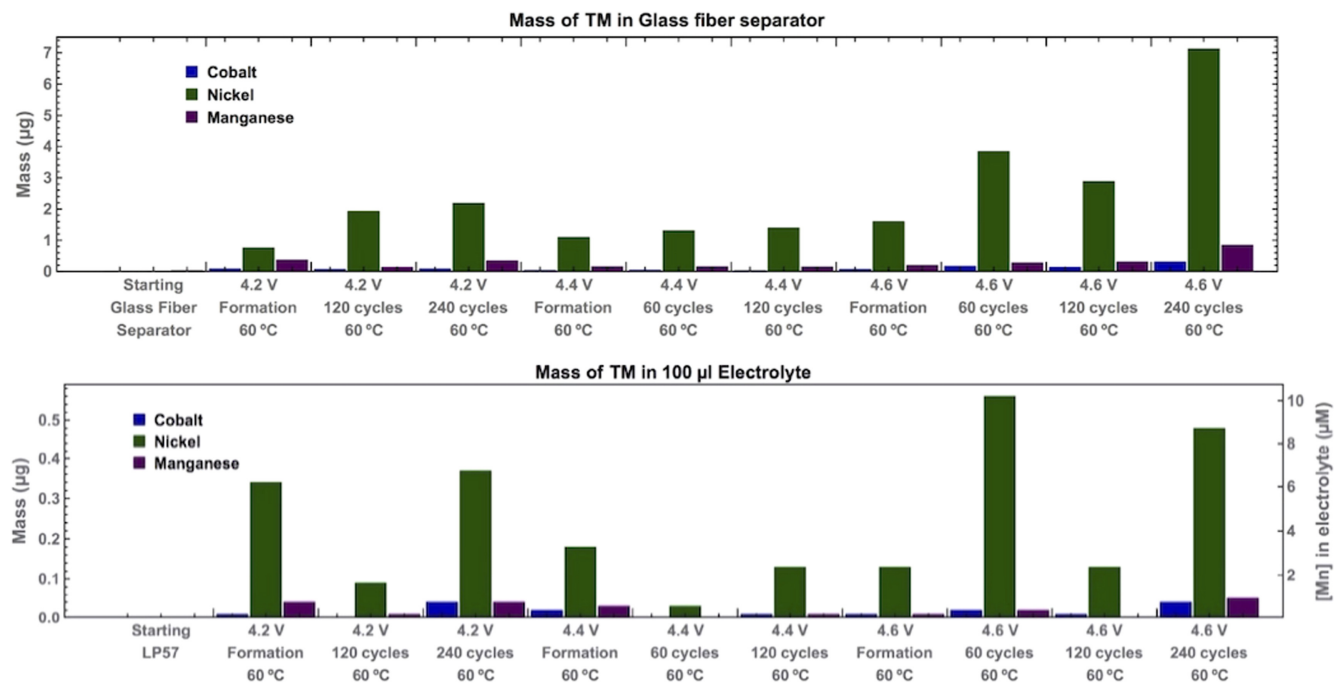


Figure 7. Mass of TM in glass fiber separator (top) and 100 μl of electrolyte (bottom) extracted from the Swagelok cells. There is an order of magnitude difference in the amount of metals in the glass fiber and 100 μl of electrolyte. Note the scale of the top chart is an order of magnitude greater than the bottom chart.

than those cycled with CC (Figs. 8b, 8d). Interestingly, CCCV cycling decreases the amount of Fe and Cr at the anode (Figs. 8c, 8e), possibly indicating that the voltage hold may have a passivating effect on the corrosion.

Impact of cell format: Swagelok vs Coin vs Pouch.—To understand how representative the results from the flooded Swagelok cells are, we compare the Swagelok measurements to two more conventional cell formats, coin cells with the same electrodes as the Swagelok cells and a small pouch cell which does not contain any stainless steel components. The pouch cell cathode contains the same NMC811 powder, but a different binder and conductive carbon. The pouch cells also have a different graphite anode and contain only a single polymer separator layer. Cells in all three formats cycled with a 4.2 UCV at 60 °C using CC show significant capacity fade (Fig. 9). However, there was a difference in the cell polarization between the Swagelok/coin cells and the pouch cell. The higher polarization of the pouch cell is attributed to the approximately two times greater loading of NMC811 in the pouch cell (16.7 mg cm^{-2} , single-sided) compared to the electrodes used in the Swagelok and coin cells (8.3 mg cm^{-2}). The higher polarization also accounts for the lower capacity of the pouch cell in the initial aging cycles (Fig. 9). We note that while the ageing studies were performed with a lower cut-off voltage of 3.0 V, an additional discharge was performed for the pouch cell after the ageing cycles were completed from 3.0 V to 2.0 V before it was disassembled, where 9.2 mAh g^{-1} of additional discharge capacity was extracted (Table SI). This additional discharge capacity is included in the electrochemical measurements presented in Table I and should be considered when comparing the results from the three cell formats.

The coin cell anode has more deposited cathode metals than the Swagelok and pouch cell anodes. This is in part (specifically the nickel and manganese deposits) due to the additional corrosion of the stainless steel coin cell body, since the coin cell anode also had more deposits of chromium and iron than the Swagelok cell anode. Note that the pouch cells contain two times higher mass loadings of the cathode vs the other cells, and thus, strictly, to

compare the deposited cathode metals, per mass of cathode per area, with the other cells, the measured deposited cathode metals should be divided by two. The low amounts of iron and chromium are consistent with the absence of stainless steel in the pouch cell and the amounts of aluminum, iron and chromium measured in the pouch cell after cycling were all similar to the values measured for the pristine anode (Fig. S8). Because the pouch cells do not have any additional sources of nickel and manganese apart from the nickel tab fused to the copper current collector, ratios of the deposited metals at the anode directly reflect the cathode metal dissolution. The lower Ni/Mn ratio of 2.2 in comparison to that in NMC811 clearly indicates preferential Mn dissolution when charged to 4.2 V and furthermore confirms that at least some of the Ni seen in other cell formats under these conditions originates from the stainless components.

Discussion

Capacity fade at stressed conditions.—At higher temperatures and UCVs, cell capacity fade in NMC811 cells cannot simply be captured by lithium-ion trapping in the SEI. In these conditions, cell polarization and electrolyte oxidation increase the complexity of the interpretation. While previously, the amount of trapped lithium has been measured directly using ICP⁷ or estimated via dQ/dV analysis,^{25,26} here we use XRD analysis of the cathodes to directly determine the lithium concentration in the cathode. Lithium ICP measurement of the anodes in this work were not meaningful, since the electrolyte salts were not rinsed from the electrodes before the acid treatment; furthermore, washing can potentially (partially) remove the SEI.

Comparing the results from the electrochemistry and diffraction measurements of the SoC of the discharged cells in Table I, the best agreement between the two techniques occurs for cycling performed at room temperature and lower UCVs, conditions where the cell does not experience significant cell polarization by cycle 120 (Fig. 3) and will undergo fewer electrolyte side reactions at the cathode.^{4,16,27} Under these cycling conditions, the capacity fade occurs predominantly via lithium trapping in the SEI layer, as was found in other

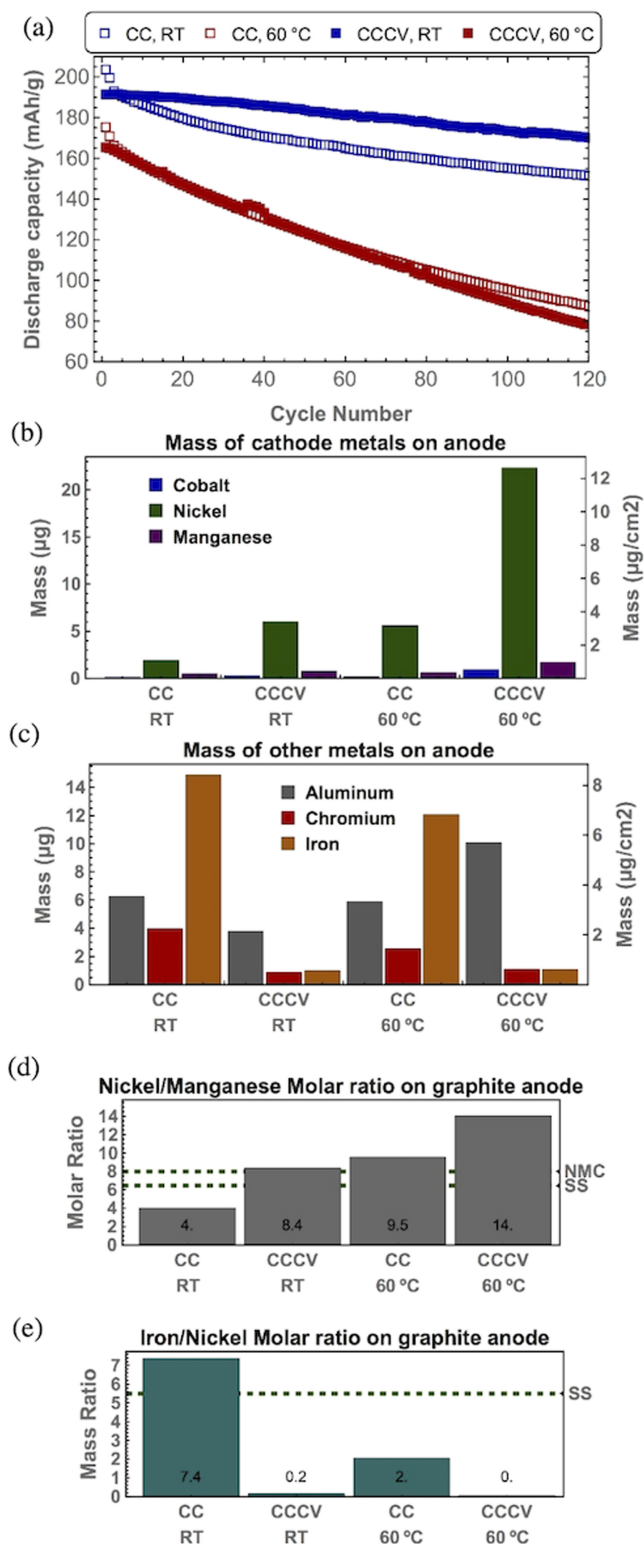


Figure 8. Comparison of discharge capacity fade (top), mass of cathode metals at the anode and metal ratios in Swagelok cells cycled to 4.4 UCV using CC vs CCCV at room temperature and 60 °C.

studies with these electrodes.²⁵ However, when the capacity fade based on the electrochemistry and cathode SoC measured using diffraction differ significantly, this indicates that the loss of lithium inventory (estimated based on x_{XRD}) cannot account for the capacity fade fully and there must be additional contributions. Furthermore, the significant increase in cell polarization (generally attributed to an

increase in the charge transfer resistance at the cathode-electrolyte interface)³ indicates that further degradation mechanisms occur during cycling at stressed conditions. The degree of cell polarization in the cells cycled at the stressed conditions typically takes thousands of cycles to reach (i.e., many months to years) in cells cycled at room temperature and lower UCVs, but was here was achieved in weeks allowing the consequences of these stressed conditions on TM metal dissolution to be explored in a reasonable timeframe.

Distribution of metals throughout the cell.—Metals from the cathode and the cell casings are deposited on all the substrates and components investigated, the amount of TMs being highest in the anode, and similar amounts found on the separator and in the electrolyte reservoir in the Swagelok cells. To further understand the accumulation of metals on the anode rather than in the electrolyte, we estimated the diffusion length of metals (D_L) in the cells during cycling. Assuming the metal complexes have transport values that are of the same order of magnitude to the Li^+ ions in carbonate solvents,^{28,29} during a single aging cycle (~6 h) the metal ions will diffuse on the millimetre length-scale ($D_{\text{Li}^+} \sim 10^{-10} \text{m}^2/\text{s}$, $D_L = \sqrt{6D_{\text{TM}}t}$, for three dimensional diffusion), enough for metals to migrate from the cathode to the anode, but not enough to reach the reservoir in the flooded Swagelok cell geometry. However, over the time it takes for the cell to undergo the cell aging (> 60 cycles), the transition metal ions can be expected to reach the reservoir, and electrolyte extracted from measurements performed on this timescale should reflect the overall metal concentration in the electrolyte.

Ni^{2+} , Mn^{2+} and Co^{2+} have limited solubilities in battery carbonate electrolytes when complexed with a variety of anions (fluoride,³⁰ acetylacetonate¹⁴) and can simply precipitate out on the anode and the separator. However, Ni^{2+} , Mn^{2+} and Co^{2+} ions also can all be reduced electrochemically to the metallic state at potentials well above 1 V vs Li/Li^+ in LP57 on carbon electrodes.¹⁰ The fact that the anode has a substantially higher amount of TM deposits than the separator and electrolyte suggests that there is a driving force for TM deposition on the anode (Fig. 5), suggests that the SEI is not acting as a significant barrier to continued metal deposition on the anode as it continues to thicken. However, the process of metal deposition on/in the SEI is complex because metal ions can (a) precipitate as salts with electrolyte degradation products (replacing Li^+), (b) be electrochemically reduced to the metallic state where they can act as catalysts for electrolyte decomposition reactions¹⁹ or (c) simply precipitate with the anion due to saturation.

The gradual increase of metals with cycle number on the glass fiber separator is indicative of the limited solubility in the electrolyte by the cathode and cell casing ions resulting from an electrochemically driven processes at the cathode or cell casings/current collectors (as discussed below). The glass fiber separators (Whatman GF/B) are designed as “high loading capacity” particulate filters, so it is reasonable to expect them to capture a large mass of poorly soluble compounds. Electrolytes extracted from cells assembled and not cycled (left at open circuit without forming) had only slightly higher concentrations of transition metals after calendar ageing (and very little metal deposition on the anode) reinforcing that there is limited solubility of the metal ions in the electrolyte (Fig. S9).

TM dissolution and cell voltage.—This study shows a strong correlation between cathode metals at the anode and UCV during CC cycling as highlighted in Figs. 4 and 5, with higher UCV leading to more TM deposition. Furthermore, when a CCCV protocol is used, the voltage hold increases not only the total time that the cathode is held at the UCV, but also increases the average SoC of the NMC particles, since the NMC particles continue to delithiate, shown clearly here to cause an increased amount of TM deposition on the anode.

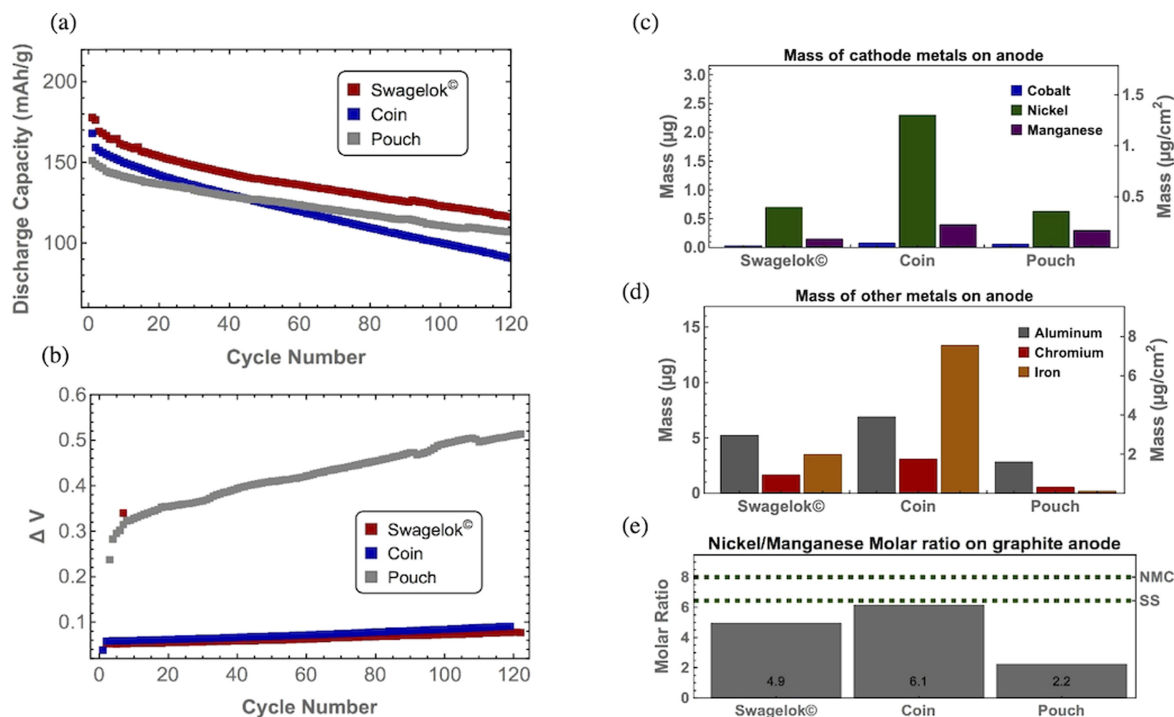


Figure 9. Impact of cell format on capacity fade, cell polarization and metal deposition on anode for cells cycled at 60 °C for 120 cycles with a 4.2 V UCV.

A manganese to nickel to cobalt ratio for the deposits at the anode that differs from that in NMC811 has been observed previously for NMC811 cathodes at room temperature where preferential dissolution of manganese was observed.⁸ Our results show an increase in the Ni/Mn ratio for cells cycled under stressed conditions, indicating increased nickel dissolution and suggesting that there are multiple mechanisms for TM dissolution in NMC811 cathodes. While nickel and manganese are also products of stainless steel corrosion, based on the masses of the majority stainless component (Fe) and the Fe/Ni ratio, corrosion of SS cannot be the primary mechanism responsible for the increase in nickel deposition.

Cell format and metal dissolution.—In addition to the TM dissolution from the NMC cathode, there are significant deposits of metals (Cr, Fe, Ni, Mn) from SS in the Swagelok and coin cell formats, SS being present in the electrode contacts and cell casings. While the flooded Swagelok cells have the largest contact area between the electrolyte and the SS casing and current collectors, more corrosion was actually seen in the coin cell, where the electrolyte to SS interface primarily arises from the electrode contacts. The iron content was noticeably higher for the coin cell (Fig. 9), which suggests that the difference may be due to the different grades of stainless used in the coin (304) and Swagelok (316) cells.

The source of metals from the SS casings complicates the interpretation of the Swagelok and coin cells and motivated the testing of pouch cells, which are packaged in polymer coated aluminum. The pouch cell anode had noticeably fewer cathode metal deposits (for a 4.2 V UCV and at 60 °C), than both the Swagelok and coin cell anodes. Minor amounts of iron and chromium were seen, but these were already present in the graphite anode before cycling (Fig. S8). The smaller mass of cathode metals (per mass of cathode material per area) is likely due to three reasons. First is the simple absence of the stainless steel in the pouch cell as an additional source of nickel and manganese. Second, the pouch cells were more polarized, which decreases the average SoC at the cathode at the UCV (a similar phenomenon was seen when comparing the cells cycled using CC vs CCCV, where the former had fewer cathode deposits). Finally, the decreased metal deposits on

the pouch cell anode may simply highlight the benefits of building cells on a pilot manufacturing line, rather than in an academic laboratory.

Mechanisms for metal dissolution/corrosion.—Given the large differences in capacity loss for the different cells as a function of UCV, temperature and cell design, we now attempt an order of magnitude estimate of the electrons consumed by the various corrosion processes. Assuming that the reduction of dissolved M^{2+} cathode ions at the anode to M^0 consumes two electrons, for the 4.6 UCV, 60 °C, 240 cycles cell, this corresponds to 3.6 mAh g^{-1} (1.8% of 195 mAh g^{-1} , capacity) for the total Ni, Mn, and Co deposited on the anode. For simplicity, presuming the Fe, Al and Cr are present as M^{3+} , a further 2.5 mAh g^{-1} (1.2%) is consumed on the anode for the same cell. (For completeness, the loss of active mass of the cathode due to dissolution would correspond to a capacity loss of approximately 0.5% or approx. 1.0 mAh g^{-1}). These numbers are much lower than the total lithium lost to the SEI, and thus the metal oxidation/reduction reactions cannot directly contribute to coulombic inefficiencies—unless via redox shuttle processes. Rather, the metals observed are associated with, or are causes of the coulombic inefficiencies. Although these redox processes are small in comparison to the total capacity fade, they may be an important consideration for optimizing cells where other contributions to capacity fade have been reduced. We now discuss the implications and possible mechanisms that occur in these cells, before discussing how they may (and have been proposed) to occur.

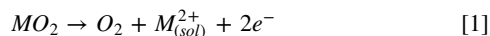
Metal loss from the cathode can occur via two processes, chemical, where no electrons are consumed and electrochemical, where the formation of a dissolved ion is a consequence of electron flow. M^{2+} ions generally have higher solubilities and labilities than their oxidised counterparts in non-aqueous electrolytes, Mn^{2+} , and Co^{2+} being the most labile, given their small crystal field stabilization energies in octahedral (and other) environments. Ni^{2+} , as a d^8 ion, is the least labile.³¹ Furthermore, the role of the Jahn-Teller (JT) active ion Mn^{3+} in promoting dissolution has also been discussed,³² and Ni^{3+} dissolution should not be discounted. Manganese dissolution is generally thought to occur via a disproportionation mechanism if Mn^{3+} is present, forming Mn^{2+} that dissolves with Mn^{4+}

remaining in the cathode.¹³ This mechanism is less likely for NMC811, particularly at high SoC, unless it occurs as part of a coupled electrochemical process involving oxidation of another species (e.g., the electrolyte or the oxide ions). While dissolution of all these ions is expected to be more pronounced at high temperatures, increased dissolution at 4.6 V via a simple dissolution mechanism is more likely if high voltages trigger another mechanism that indirectly promotes dissolution.

Electrolyte degradation has been proposed to promote dissolution via the generation of HF or other acid species^{33,34} (generally from PF₆⁻ degradation reactions³⁵—often involving water¹⁸), or possibly via the creation of organic anions that chelate the metal ions, a mechanism proposed for lithium manganates.¹⁴ At least for lithium cobalt oxide, our previous work suggests that electrolyte oxidation is a chemical process resulting from, for example, attack by reactive oxygen species such as singlet oxygen.³⁶ Direct electrochemical oxidation has, however, not been ruled out yet for this system and coupled catalytic processes involving TM metal reduction and electrolyte oxidation have been proposed previously.³⁷ Oxygen loss at high voltages,⁴ possibly via the formation of singlet oxygen³⁸ in addition to promoting electrolyte degradation, removes oxide anions from the lattice, reducing the coordination number of the surface metal ions, and likely driving dissolution. Rock salt phase-transitions at the particle surface^{17,22,39} result from this mechanism and may be an indirect source of metal dissolution. Finally, particle cracking^{40,41} increases the cathode surface area and thus helps promote dissolution.

To assess whether the TM dissolution involves electrochemical reactions or not, here, we compare the cumulative capacity loss (the irreversible capacity loss within one cycle summed over all cycles, Table SII) and x_{XRD} , the former being indicative of the coulombic inefficiency throughout the cycling and the latter providing an estimate of the lithium inventory loss. For example, we consider the electrochemical measurements for 4.4 UCV, 60 °C, 120 cycle CCCV cell. The cumulative capacity results indicated that a total of 0.61 more electrons per formula unit were consumed on charge than on discharge (corresponding to 168.3 mAh g⁻¹ of cumulative capacity loss), which, if the only degradation process is anode slippage and Li trapping in the SEI, would imply that the cathode lithium content of the fully discharged cell is Li_{0.39}Ni_{0.8}Mn_{0.1}Co_{0.1}O₂. However, the XRD indicated that only 0.37 Li ions were removed, i.e., 0.24 electrons have been consumed by additional processes that occur on charging. This result strongly suggests that the degradation mechanisms at high UCV originate from an electrochemical process (i.e., they consume electrons); the consequent effect on for example electrolyte oxidation or cathode degradation (e.g., by rock salt formation) may then be either direct (i.e., electrochemical) or indirect (chemical). Note that some additional discharge capacity may be obtained on discharging to 2.0 V (as done for the pouch cell (see Table I)), but for the pouch cell, this corresponds to only approximately 9 mA g⁻¹ or 0.03 electrons.

The observation of deposits of cathode metals all over the cell, not just at the anode, suggests that the metals do not simply dissolve. Rather, the dissolution involves a mechanism that drives supersaturation of the metals in one location and precipitation elsewhere. A simple (illustrative) mechanism to produce metal dissolution can be written as follows:



We recognize that there are many such mechanisms (including potentially loss of M^{3+/4+} ions) and that rock salt formation, rather than metal dissolution, is likely to be the dominant product of oxygen loss. The oxygen loss reactions, while accelerated at high temperatures and higher UCVs are present even at ambient temperatures and an UCV of 4.2 V.

Metals are often thought to promote electrolyte degradation at the anode.^{7,10,11,35} The steady lithium loss (indicated by the XRD analysis, Table I) shows that SEI formation continues with further cycling, and at room temperature, although it is certainly accelerated

at higher UCVs. Surprisingly, the effect is less pronounced at higher temperatures, suggesting that additional side reactions occurring during formation (which also occurred at 4.6 V) may simply be masking the additional SEI formation or an oxidation process at the cathode, replenishing the lithium inventory.⁸

Finally, the 4.2 V pouch cell data suggests that a well-balanced cell with no additional metals from corrosion of the cell casings has significantly less lithium loss (beyond the formation cycle). Experiments are now in progress to explore higher UCVs in the pouch cells. Like Swagelok and coin cells, cylindrical cell formats are encased in steel, motivating further studies to understand the effect of cell packaging on anode metal deposits and any subsequent cell degradation. In addition, both cylindrical and pouch cell formats often have nickel tabs at the anodes, which introduce an additional source of TMs. Understanding the impact of the dissolution of these metal components and their deposition on the anode could be instructive for understanding capacity fade in commercial cells.

Conclusions

In this work, we investigated the degradation and TM dissolution of NMC811/graphite cells at stressed cycling conditions, namely elevated temperatures (60 °C) and high upper cutoff voltages (4.4 V and 4.6 V) in three cell formats (Swagelok, coin and pouch cells). The experiments were contrasted with those performed at milder conditions (room temperature and 4.2 UCV). By cycling cells at stressed conditions, we were able to replicate the cell polarization induced by side reactions and mechanical stresses that can typically take thousands of cycles (i.e. many months to years) to achieve in weeks, allowing the effects of this on metal dissolution to be investigated on a reasonable timeframe.

To understand cell capacity loss based on the electrochemical measurements, they were compared with lithium contents extracted from diffraction measurements of the cathodes in the discharged state via structural refinements. The latter can be directly associated with the loss of lithium inventory (i.e., the Li trapped at the anode). Under stressed cycling conditions, the lithium loss alone could not explain the capacity fade and the increased cell polarization contributed to the reduced capacity, for cells cycled at C/3. However, at room temperature and 4.2 UCV, the capacity fade could largely be ascribed to lithium loss to the SEI at the anode, as observed previously.²⁵

The mass of cathode metal deposits on the graphite anode was strongly dependent on the cycling temperature, UCV, and number of cycles for CC cycling. Cells held at constant voltage at the top of charge (CCCV) had significantly more cathode metals deposited on the anodes than those cycled using CC only, showing that increasing the time that the cathode is held at high voltages drives TM dissolution. Interestingly, the mass of TM metals in the electrolyte did not change significantly with cycling condition and UCV, presumably limited by the solubility of the ions in the electrolyte. Significantly higher concentrations of TM are observed on the anode following cycling, which clearly indicates the driving force for metal deposition.

Along with metals originating from the cathode, we identified significant metal deposits at the anode originating from stainless steel, occurring in cells even when cycled to lower UCVs (e.g., 4.2 V). In contrast to the increased amount of dissolution from the cathode with the UCV, no clear correlation is observed for the dissolution of stainless steel. This phenomenon has been less carefully analyzed and discussed in the literature and yet in certain commercial cell is likely to occur. The use of pouch cells, clearly reduces this phenomenon.

Our study provides baseline data as well as insight into ageing conditions that result in increased degradation and metal dissolution. Finally, we hope that the stressed conditions and the resulting accelerated degradation studied here, provide a potential method for exploring the mechanisms driving TM dissolution, cathode polarization and capacity fade, on reasonable experimental timescales.

Acknowledgments

We thank Ms. Jennifer Allen, Prof. Mary Ryan and Dr Daniel Abraham for helpful discussions. We thank Stephen Young and Nigel Howard for assistance with the ICP-OES measurements. This work is supported by the Faraday Institution under grant no. FIRG001.

ORCID

Zachary Ruff  <https://orcid.org/0000-0001-9097-3735>

Chao Xu  <https://orcid.org/0000-0001-5416-5343>

Clare P. Grey  <https://orcid.org/0000-0001-5572-192X>

References

- W. Li, E. M. Erickson, and A. Manthiram, *Nat. Energy*, **5**, 26 (2020).
- J. Li, L. E. Downie, L. Ma, W. Qiu, and J. Dahn, *J. Electrochem. Soc.*, **162**, A1401 (2015).
- J. A. Gilbert, J. Bareño, T. Spila, S. E. Trask, D. J. Miller, B. J. Polzin, A. N. Jansen, and D. P. Abraham, *J. Electrochem. Soc.*, **164**, A6054 (2016).
- R. Jung, M. Metzger, F. Maglia, C. Stinner, and H. A. Gasteiger, *J. Electrochem. Soc.*, **164**, A1361 (2017).
- L. Ellis, J. Allen, L. Thompson, J. Harlow, W. Stone, I. Hill, and J. Dahn, *J. Electrochem. Soc.*, **164**, A3518 (2017).
- J. W. Braithwaite, A. Gonzales, G. Nagasubramanian, S. J. Lucero, D. E. Peebles, J. A. Ohlhausen, and W. R. Cieslak, *J. Electrochem. Soc.*, **146**, 448 (1999).
- J. A. Gilbert, I. A. Shkrob, and D. P. Abraham, *J. Electrochem. Soc.*, **164**, A389 (2017).
- M.-T. F. Rodrigues, K. Kalaga, S. E. Trask, I. A. Shkrob, and D. P. Abraham, *J. Electrochem. Soc.*, **165**, A1697 (2018).
- L. Thompson, W. Stone, A. Eldesoky, N. Smith, C. M. McFarlane, J. Kim, M. Johnson, R. Petibon, and J. Dahn, *J. Electrochem. Soc.*, **165**, A2732 (2018).
- R. Jung, F. Linsenmann, R. Thomas, J. Wandt, S. Solchenbach, F. Maglia, C. Stinner, M. Tromp, and H. A. Gasteiger, *J. Electrochem. Soc.*, **166**, A378 (2019).
- T. Joshi, K. Eom, G. Yushin, and T. F. Fuller, *J. Electrochem. Soc.*, **161**, A1915 (2014).
- K. Leung, *Chem. Mater.*, **29**, 2550 (2017).
- J. C. Hunter, *J. Solid State Chem.*, **39**, 142 (1981).
- A. Jarry, S. Gottis, Y.-S. Yu, J. Roque-Rosell, C. Kim, J. Cabana, J. Kerr, and R. Kostecki, *JACS*, **137**, 3533 (2015).
- M. Evertz, F. Horsthemke, J. Kasnatscheew, M. Börner, M. Winter, and S. Nowak, *J. Power Sources*, **329**, 364 (2016).
- R. Jung, M. Metzger, F. Maglia, C. Stinner, and H. A. Gasteiger, *The Journal of Physical Chemistry Letters*, **8**, 4820 (2017).
- F. Lin, I. M. Markus, D. Nordlund, T.-C. Weng, M. D. Asta, H. L. Xin, and M. M. Doeff, *Nat. Commun.*, **5**, 1 (2014).
- D. Strmcnik et al., *Nat. Catal.*, **1**, 255 (2018).
- S. Solchenbach, G. Hong, A. T. S. Freiberg, R. Jung, and H. A. Gasteiger, *J. Electrochem. Soc.*, **165**, A3304 (2018).
- J. E. Harlow, X. Ma, J. Li, E. Logan, Y. Liu, N. Zhang, L. Ma, S. L. Glazier, M. M. Cormier, and M. Genovese, *J. Electrochem. Soc.*, **166**, A3031 (2019).
- K. Märker, P. J. Reeves, C. Xu, K. J. Griffith, and C. P. Grey, *Chem. Mater.*, **31**, 2545 (2019).
- C. Xu, K. Märker, J. Lee, A. Mahadevegowda, P. J. Reeves, S. Day, M. F. Groh, S. P. Emge, C. Ducati, B. Layla Mehdi, C. C. Tang, and C. P. Grey, *Nature Materials*, **20**, 84 (2021).
- T. Ohzuku, Y. Iwakoshi, and K. Sawai, *J. Electrochem. Soc.*, **140**, 2490 (1993).
- J. Vetter, P. Novák, M. R. Wagner, C. Veit, K. C. Möller, J. O. Besenhard, M. Winter, M. Wohlfahrt-Mehrens, C. Vogler, and A. Hammouche, *J. Power Sources*, **147**, 269 (2005).
- W. M. Dose, C. Xu, C. P. Grey, and M. F. L. De Volder, *Cell Reports Physical Science*, **1**, 100253 (2020).
- I. Bloom, A. N. Jansen, D. P. Abraham, J. Knuth, S. A. Jones, V. S. Battaglia, and G. L. Henriksen, *J. Power Sources*, **139**, 295 (2005).
- E. Logan, H. Hebecker, X. Ma, J. Quinn, Y. HyeJeong, S. Kumakura, J. Paulsen, and J. Dahn, *J. Electrochem. Soc.*, **167**, 060530 (2020).
- C. L. Berhaut, D. Lemordant, P. Porion, L. Timperman, G. Schmidt, and M. Anouti, *RSC Adv.*, **9**, 4599 (2019).
- J. Landesfeind and H. A. Gasteiger, *J. Electrochem. Soc.*, **166**, A3079 (2019).
- A. Banerjee, Y. Shilina, B. Ziv, J. M. Ziegelbauer, S. Luski, D. Aurbach, and I. C. Halalay, *JACS*, **139**, 1738 (2017).
- J. E. Huheey, E. A. Keiter, R. L. Keiter, and O. K. Medhi, *Inorganic Chemistry: Principles of Structure and Reactivity* (Pearson, India) (2006).
- A. Manthiram, *Nat. Commun.*, **11**, 1 (2020).
- M. Metzger, B. Strehle, S. Solchenbach, and H. A. Gasteiger, *J. Electrochem. Soc.*, **163**, A798 (2016).
- C.-Y. Li, Y. Yu, C. Wang, Y. Zhang, S.-Y. Zheng, J.-F. Li, F. Maglia, R. Jung, Z.-Q. Tian, and Y. Shao-Horn, *The Journal of Physical Chemistry C*, **124**, 4024 (2020).
- S. Solchenbach, M. Metzger, M. Egawa, H. Beyer, and H. A. Gasteiger, *J. Electrochem. Soc.*, **165**, A3022 (2018).
- B. L. Rinkel, D. S. Hall, I. Temprano, and C. P. Grey, *JACS*, **142**, 15058 (2020).
- M. Jiang, B. Key, Y. S. Meng, and C. P. Grey, *Chem. Mater.*, **21**, 2733 (2009).
- J. Wandt, A. T. Freiberg, A. Ogrodnik, and H. A. Gasteiger, *Mater. Today*, **21**, 825 (2018).
- J. Li, H. Liu, J. Xia, A. R. Cameron, M. Nie, G. A. Botton, and J. Dahn, *J. Electrochem. Soc.*, **164**, A655 (2017).
- H.-H. Ryu, K.-J. Park, C. S. Yoon, and Y.-K. Sun, *Chem. Mater.*, **30**, 1155 (2018).
- T. M. M. Heenan et al., *Adv. Energy Mater.*, **10**, 2002655 (2020).